Zinc phthalocyanine conjugated cellulose nanocrystals for memory device applications

Chaulagain, Narendra; Alam, Kazi M.; Kumar, Pawan; Kobryn, Alexander E.; Gusarov, Sergey; Shankar, Karthik

Publisher's version / Version de l'éditeur:
https://doi.org/10.1088/1361-6528/ac2e78
Nanotechnology, 33, 5, pp. 1-9, 2021-11-08

Zinc Phthalocyanine Conjugated Cellulose Nanocrystals for Memory Device Applications

Narendra Chaulagain[1], Kazi M. Alam[1,2], Pawan Kumar[1], Alexander E. Kobryn[2], Sergey Gusarov[2], and Karthik Shankar[1*]

[1] Department of Electrical and Computer Engineering, University of Alberta, Edmonton, AB T6G 1H9, Canada

[2] Nanotechnology Research Centre, National Research Council Canada, 11421 Saskatchewan Drive, Edmonton, AB T6G 2M9, Canada
*Corresponding author's email addresses: kshankar@ualberta.ca

Abstract

We present the electrical properties of zinc phthalocyanine covalently conjugated to cellulose nanocrystals (CNC@ZnPc). Thin films of CNC@ZnPc sandwiched between two gold electrodes showed pronounced hysteresis in their current-voltage characteristics. The layered metal-organic-metal (MOM) sandwich devices exhibit distinct high and low conductive states when bias is applied, which can be used to store information. Density functional theory (DFT) results confirmed wave function overlap between CNC and ZnPc in CNC@ZnPc, and helped visualize the lowest (LUMO) and highest molecular orbitals (HOMO) in CNC@ZnPc. These results pave the way forward for all-organic electronic devices based on low cost, earth abundant CNCs and metallophthalocyanines.

1. Introduction

The advent of the era of big data has seen an explosion in the amount of global digital information over the past few years. Concurrently, the availability of cheap, low-power, relatively stable sensing, memory and computing products is growing. With the rapid development of the Internet of Things (IoT), memory devices are desired to be mechanically flexible, bio-friendly, and even implantable for personal healthcare and smart medical equipment [1]. Conventional silicon-based semiconductor devices have serious downscaling constraints related to data fidelity, heat death, and large manufacturing costs thus motivating the design and physical realization of elective data capacity gadgets made from new materials to meet the needs of future microelectronics. Organic materials display solid potential to be used in the active layers of electronic devices. There is a worldwide effort in both corporate and academic labs to create new memory devices combining the best characteristics of today's dominant technologies [2]. It is not possible to grow single crystals on top of amorphous substrates which limits the growth of several effective memory layers on a single wafer and constitutes one of the major hurdles in scalable device fabrication based on single-crystal semiconductor technologies. Memory devices fabricated using organic materials enable low-temperature film deposition on flexible, polymeric substrates [3]. This helps in the deposition of multiple layers, increasing the density per given feature size. At ambient temperature, organic compounds can be dispensed cheaply and over vast areas on plastic, glassware, and metal foils. Devices such as organic field-effect transistors (OFET), organic light-emitting diodes (OLED) and organic photovoltaics (OPV) have been the focus of intense research, but electronic memory using organic materials is still in the exploration stage [4]. In most organic memory devices, organic semiconductor layers are sandwiched between two metal electrodes [5]. Herein, we explain a memory effect in a thin film device based on organic materials which have the potential to precedence over existing memory devices as the material has the basic requirements for binary information storage and presents the potential for organic memory applications. To store information, memory devices make use of hysteresis in the electrical characteristics in response to an external field. Studying the actual hysteresis of the device helps to recover the stored data. It is noteworthy that piezoelectric materials typically exhibit hysteresis in their electric polarization as a function of applied bias. Self-assembled films of cellulose nanocrystals (CNCs) exhibit a large piezoelectric effect even in the absence of external poling.

Zinc phthalocyanine (ZnPc) is a metal-complexed heteroaromatic molecule which is part of the metalloporphyrin class with charge carriers delocalized over the macrocycle [6]. It manifests π-conjugated structure and shows structural self-organization characteristics due to π-stacking [7, 8]. ZnPc is a well-known *p*-type organic semiconductor which is used as a hole transporter and active layer in OPVs, OLEDs and OTFTs [9-11]. CNCs have been used as a morphology-modifying additive to enhance charge transport in organic semiconductor thin films . CNC-ZnPc conjugates have been used in fluorescence sensing of volatile organic compounds [12]. Solution processed ZnPc@CNC thin film memory devices are introduced in this work.

* Tel: 780-492-1354; email: kshankar@ualberta.ca

2. Methodology

a. Computational details

Theoretical calculations were performed using a combination of classical and quantum mechanical approaches. First, a large segment of Na-CNC was constructed comprising cellulose nanofibrils of type I β phase (according to XRD results discussed later), which was optimized using classical molecular dynamics (MD). Periodic boundary condition was considered in this computational step which was performed in LAMMPS (Large-scale Atomic/Molecular Massively Parallel Simulator) with COMPASS (Condensed-phase Optimized Molecular Potential for Atomistic Simulation Studies) force field [13-15]. A small portion of the MD-optimized system containing Na-CNC hydrophilic plane ($1\bar{1}0$) was considered for the second step of calculations employing a quantum chemical approach based on density functional theory (DFT). This ($1\bar{1}0$) plane was kept intact to simulate an environment where the large MD-optimized background would be present. The O atom of the Na-CNC surface (from -OH) was included in the covalent conjugation, and some of the O atom's neighboring atoms of the CNC side plane remained relaxed. On the other hand, the entire ZnPc molecule was fully relaxed during geometry optimization. ZnPc molecules were attached both horizontally and vertically on the Na-CNC surface. DFT computations for the pure zinc phthalocyanine plus its conjugate with Na-CNC were performed using OpenMX 3.8 (Open source package for Material eXplorer) platform, where pseudo-atomic localized basis functions and norm-conserving pseudopotentials are implemented [16, 17]. General gradient approximation (GGA) with Perdew–Burke–Ernzerhof (PBE) exchange-correlation functional was considered in the computational version [18]. We have chosen dispersion-corrected functional to account for the long-range electron correlations [19], particularly the DFT-D2 method has been considered in all the calculations. These corrections are important since cellulose nanocrystals are characterized by Van der Waals interactions, such as London dispersion forces, dipole-dipole forces and hydrogen bonds [20, 21]. The energy cut-off value and the threshold for convergence criterion for a self-consistent loop were set to be 220 eV and 5×10^{-5} respectively. Gaussian broadening method was employed for the construction of projected density of states (PDOS) plots, with broadening function's half-width, S set to 0.08 eV. Electron density difference isosurfaces and molecular orbitals (HOMO and LUMO) were plotted using VMD (visual molecular dynamics) visualization software. The isosurface value for the electron density difference plots was taken to be 0.015 eV Å^{-3}.

b. Experimental details

- Synthesis of materials

The sodiated sulfate form of cellulose nanocrystals (Na-CNC) was supplied by FPInnovations Inc. The detailed synthesis protocol for pristine octacarboxylated phthalocyanine, ZnPc–$(COOH)_8$, and its conjugate with sodium-doped cellulose nanocrystals (ZnPc@Na-CNC) has been reported in our previous work [12]. Briefly, the conjugation protocol involves the following major steps. First lab-synthesized ZnPc–$(COOH)_8$ was reacted with thionyl chloride ($SOCl_2$) to obtain octacarbonylchloride phthalocyanine, ZnPc–$(COCl)_8$. The activated –COCl group on ZnPc–$(COCl)_8$ was reacted with –OH functional group of CNC surface to form ester linkage (–COO–). Thus, the ZnPc molecules are covalently conjugated to Na-CNC.

- Structural and physicochemical characterizations

Field emission scanning electron microscopy (FESEM) imaging. Hitachi S-4800 field emission scanning electron microscope (FESEM) was used to study the morphological features of ZnPc@Na-CNC samples. The accelerating voltage was set to 3 kV.

Transmission electron microscopy (TEM) imaging. JEOL JEM-ARM200CF was employed for imaging the ZnPc@Na-CNC samples. This tool is outfitted with a cold Field-Emission Gun and a probe Cs corrector, and a Silicon Drift detector. An acceleration voltage of 200 kV was used in this measurement. High-resolution TEM (HRTEM) files were processed with Gatan micrograph for obtaining lattice spacings.

Absorption spectroscopy. The optical properties of the pristine ZnPc and the ZnPc@Na-CNC conjugate were studied using a Perkin Elmer Lambda-900 NIR-UV (near-infrared to ultraviolet) spectrophotometer operating in the transmission mode. Pristine ZnPc and ZnPc@Na-CNC powders were dispersed in DMF, and the solutions were drop-coated on glass substrate followed by drying on a hot plate.

X-ray diffractometry (XRD). X-ray powder diffraction (XRD) patterns of bare materials and the conjugate were acquired using a Bruker D8 advance diffractometer. This tool is outfitted with a 2D detector (VANTEC-500) and has a radiation source, namely a Cu X-ray tube (Cu–Kα, $I_\mu S_\mu$, $\lambda = 0.15418$ nm) operating at room temperature at 50W.

Raman spectroscopy. Raman spectra were collected on a Raman spectrometer (Nd: YAG laser Raman Microscope, Nicolet Omega XR) with an excitation wavelength of 532 nm. An incident power of 7 mW and a 10X objective was used for all the samples. The fluorescence correction factor was set to 6. The aperture size was 50 μm while the grating spacing was 900 lines/mm.

Electrical measurement. The sample preparation before the electrical measurements involved the following steps. 25 mg/ml of bare ZnPc and ZnPc@Na-CNC composite powders were dispersed in deionized (DI) water followed by ultrasonication to obtain a homogeneous mixture. Separately, fluorine-doped tin oxide (FTO) coated glass substrates (FTO:glass) were cleaned several times by isopropyl alcohol, acetone, and DI water. The above-mentioned solutions were drop-coated on conductive FTO:glass followed by drying on a hot plate. For the top contact, 80 nm thick Au electrodes were deposited by electron beam evaporation using a circular shadow mask of 2 mm diameter. A Keithley 4200 semiconductor parameter analyzer was used to measure the steady-state and transient conductivity in the dark and under a solar simulator AM1.5 G illumination at 100 mW/cm^2. FTO was set as ground and voltages were applied to the gold contacts.

3. Results and discussions

a. Analysis of density of states and molecular orbitals

DFT calculations were employed to reveal the electronic properties of the pristine ZnPc and its conjugate with Na-CNC. Raman spectroscopic results discussed later, gave some hint of various types of aggregation of ZnPc on Na-CNC surface. Thus, we opted for both vertical and horizontal attachments of ZnPc molecules on the surface of Na-CNC. The structural stability of the ZnPc@Na-CNC composite system was theoretically investigated by analyzing the projected density of states (PDOS) of the covalently attached atoms from the two systems. As mentioned in the methodology section, the formation of the ester linkage (–COO–) involves carbon and oxygen atoms from –COOH of the phthalocyanine as well as –OH of nanocrystals. Figure 1(a) and 1(b) shows the PDOS of the conjugating atoms of ZnPc (C) and Na-CNC (O) in ZnPc@Na-CNC for two distinct scenarios – first, when the metallophthalocyanine ring is oriented vertically and second, horizontally on the ($1\bar{1}0$) Na-CNC surface. From both plots, we observe that there exists a perfect overlap between these two atoms' PDOS in terms of energy position. This overlap indicates strong covalent attachment [22], which serves as an alternate method to perform density overlap regions indicator analysis [23]. While these

plots show overlapping peaks in terms of position (x-axis), there remains a significant difference in the peak intensity (y-axis). This is consistent with the electron density difference isosurface plots shown in Figures 1(c) and 1(d). These figures reveal that the charge depletion and accumulation regions are surrounded by C and O atoms respectively, and consequently manifest more states in the unoccupied and occupied regions respectively [Figure 1(a) and 1(b)]. The frontier orbitals, such as the highest occupied molecular orbital (HOMO) and lowest unoccupied molecular orbital (LUMO) of bare ZnPc and its conjugate with Na-CNC have been presented in Figure 1 (e) and 1(f). The HOMO and LUMO are not spatially separated in the case of bare ZnPc, unlike the composite geometries, where these molecular orbitals are more localized in space. This localization is more pronounced in the vertical geometry than the horizontal configuration. Photogenerated exciton dissociation is expected to be facilitated in such an electronic structure [24].

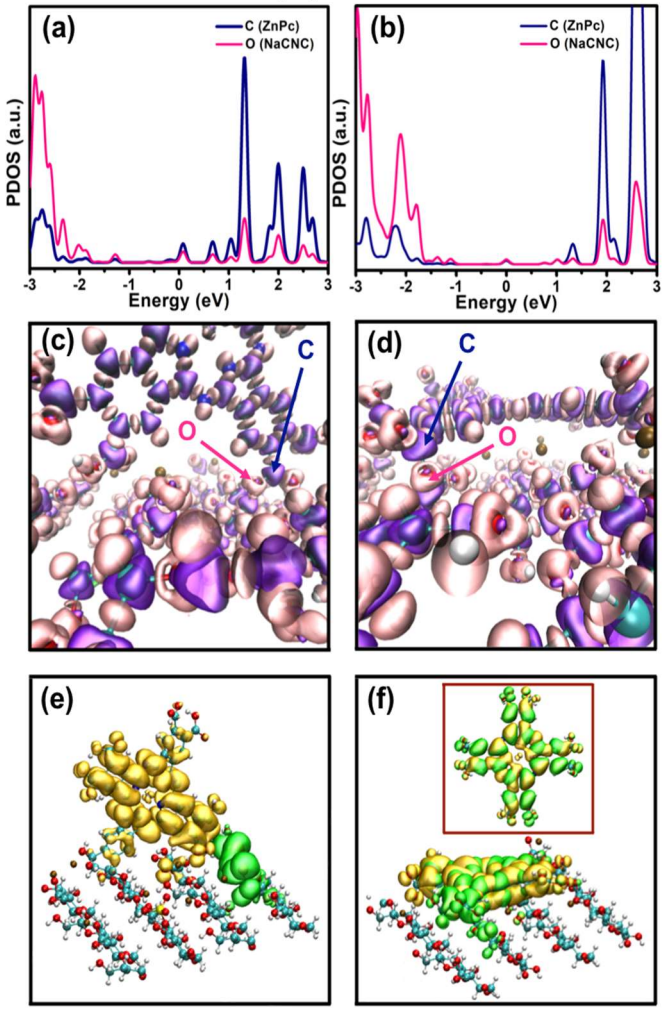

Figure 1. Projected density of states (PDOS) of the conjugating atoms of ZnPc (C) and Na-CNC (O) in ZnPc@Na-CNC, when (a) metallophthalocyanine ring is oriented vertically on the Na-CNC surface ($1\bar{1}0$) and (b) metallophthalocyanine ring is oriented horizontally on the Na-CNC surface ($1\bar{1}0$). (c) and (d) Electron density difference iso-surfaces corresponding to configurations (a) and (b) respectively. The purple- and pink-colored surfaces speak to charge consumption and collection locales individually. The iso-surface significance volume was set to 0.015 eV $Å^{-3}$. (e) and (f) Spatial distributions of molecular orbitals corresponding to configurations (a) and (b) respectively. The inset of (f) shows the spatial distributions of molecular orbitals for bare ZnPc. HOMO and LUMO are exemplified by green and yellow surfaces correspondingly. The colors for C, O, H, Na, N, and Zn atoms are cyan, red, white, ochre, blue, and pink, respectively.

b. Structural and physicochemical properties

The morphological features of the ZnPc@Na-CNC composite were studied by field emission scanning electron microscopy (FESEM). The FESEM image of the composite is presented in Figure 2(a), where a finger-like fibril morphology can be observed, distinct from rod like whiskers generally seen for stand-alone CNCs [25, 26]. Transmission electron microscopy (TEM) was employed to reveal the fine-structural features. Figure 2(b) shows the dark field TEM image of an agglomerated ZnPc@Na-CNC bundle. High-resolution transmission electron microscopy (HRTEM) image of the ZnPc@Na-CNC is shown in Figure 2(d), where the inset demonstrates the lattice plane-like ordered organization of metallophthalocyanine rings of ZnPc on the Na-CNC surface following the covalent conjugation between the two. HRTEM reveals the aggregation state of ZnPc attached to the cellulose nanocrystal surface. Compared to our previously reported work [12], we witness a more detailed aggregation behavior, which has been verified by correlating it with observed X-ray diffractogram data discussed later in this report. Figure 2(c) shows the absorption spectra for the pristine ZnPc and ZnPc@Na-CNC conjugate solid films. The optical absorption of solid films of pristine ZnPc and its conjugate with Na-CNC is shown in Figure 2(c). Compared to the liquid phase, solid-state absorption properties demonstrated distinct behavior. The octacarboxylated ZnPc can be characterized by its well-recognized Soret and Q-bands in the higher and lower energy spectral regimes respectively. The Q-band of metallophthalocyanine is a doublet with the lower energy apex at ~699 nm (corresponding to the $S_0 \rightarrow S_1$ electronic transition), and the higher energy peak at ~663 nm is characteristic of π-stacked columnar H-type aggregates [27]. Notice that while the lower energy peak in the solid-state did not change its peak position from the liquid phase, the higher energy peak shows a large redshift, due to possible enhanced aggregation in the solid phase. The doublets are reproduced in the composite with almost unchanged intensity and position, unlike in the liquid phase [12] where there was a huge intensity reduction of the lower energy peak for the composite. Unlike the liquid phase absorption behavior, the conjugate showed a much higher absorption in the Soret band region for the conjugate compared to the pristine ZnPc. However, the substantial absorption feature in the intermediate spectral region between the Soret and Q-bands is similar to the liquid state absorption results.

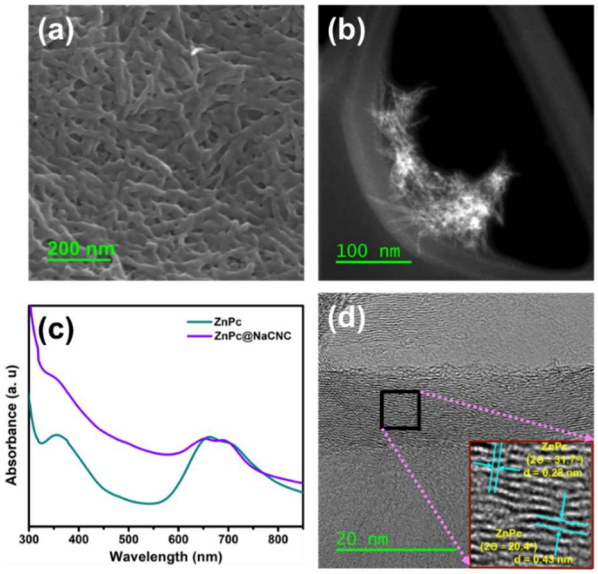

Figure 2. (a) FESEM image of ZnPc@Na-CNC. (b) Dark field TEM image of an agglomeration of ZnPc@Na-CNC. (c) UV-vis spectra of thin solid films of bare ZnPc and ZnPc@Na-CNC. (d) HRTEM image of ZnPc@Na-CNC. The inset corresponds to the selected magnified region showing lattice planes (aggregation) of ZnPc attached to the Na-CNC surface.

X-ray diffractograms (XRD) of pristine Na-CNC, pristine ZnPc, and ZnPc@Na-CNC composite are shown in Figure 3(a). The peaks at 15.2°, 16.6°, 22.6° and 34.6° correspond to the $(1\bar{1}0)$, (110), (200) and (040) planes of cellulose I [28-30]. These peaks reappeared in the conjugate assuring the unperturbed crystalline nature of the cellulose nanocrystals. The most intense and narrow peak was observed at 31.7° for pristine ZnPc. Such crystalline behavior is consistent with earlier reports involving octacarboxylated ZnPc [31]. As expected, the most intense XRD peak of bare ZnPc at 31.7° reappeared in the ZnPc@Na-CNC composite, which corresponds to *d*-spacing of 0.28 nm found in the HRTEM image discussed earlier (Figure 2d). Interestingly a new XRD peak of ZnPc at 20.4° that corresponds to a *d*-spacing of 0.43 nm (Figure 2d inset) is visible in the composite Figure 3(a). This new peak bears the signature of the conjugation-induced novel aggregation state of ZnPc on the cellulose nanocrystal surface. Figure 3(b) reveals the Raman spectra of pure Na-CNC, pristine ZnPc, and ZnPc@Na-CNC composite. The C–O–C stretching modes give rise to a vibrational peak at ~1100 cm^{-1} in cellulose, which is the dominant feature in the spectrum for the pristine Na-CNC [32, 33]. This vibrational mode also appeared in the ZnPc ZnPc@Na-CNC composite. The peaks at 666 cm^{-1} and 735 cm^{-1}, that correspond to the out-of-phase distortion of the indole bunches (moreover accepted to be coupled to the macrocycle) and coupled macrocycle-pyrrolic modes. separately [34, 35], appeared at significantly down-shifted positions of 632 cm^{-1} and 601 cm^{-1} probably because of the existence of additional –COOH classes attached to the isoindole units. The peaks appearing at 1326 cm^{-1}, 1406 cm^{-1}, and 1452 cm^{-1}, which are linked with innumerable A_1 modes in ZnPc are also noted in the conjugated ZnPc [34, 35]. However, like the low-frequency peak, all these high-frequency peaks are downshifted in the octacarboxylated ZnPc. It is interesting to note that compared to all the above-mentioned Raman modes, the most conspicuous vibrational feature of ZnPc appeared at 1514 cm^{-1} due to the out-of-phase extension of C-N-C bonds [34, 35], did not show any significant downshift, and was also fully expressed in unchanged intensity in the conjugate. All other previously mentioned Raman peaks have suppressed intensity in the conjugate compared to the pristine ZnPc. Such variation of intensity is indicative of various aggregation states of ZnPc metallophthalocyanine rings on the Na-CNC surface during the esterification and subsequent π-stacking process.

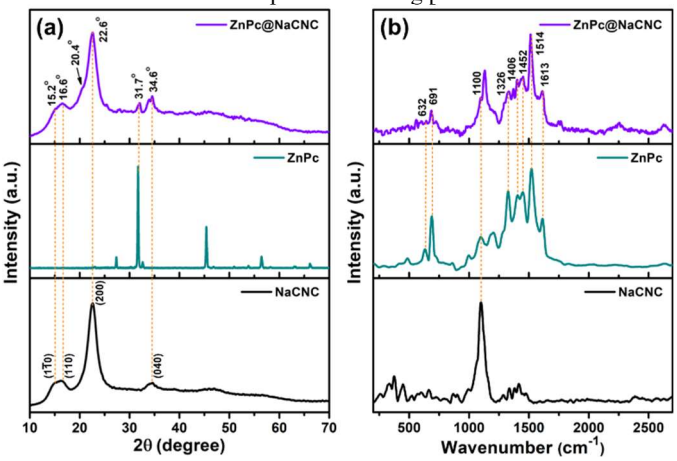

Figure 3. (a) X-ray diffractograms of bare Na-CNC, bare ZnPc, and ZnPc@Na-CNC conjugate. (b) Raman spectra of bare Na-CNC, bare ZnPc, and ZnPc@Na-CNC conjugate. Raman laser excitation wavelength was 532 nm.

c. Electrical characteristics

Electrical characterization of thin films is typically performed either using planar or sandwich devices. The sandwich configuration is more important while designing thin-film devices such as diode, memory devices, solar cells, and transistors [36]. Here we present the DC electrical characterization of ZnPc@CNC and bare ZnPc thin films by in the sandwich configuration (Figure 4(a)). ZnPc is an organic semiconductor with an exciton binding energy > 300 meV [37, 38].

Ohmic or hopping conduction is expected in a device with metal/ZnPc/metal structure wherein a *p*-type organic semiconductor material with low mobility and high thermal activation energy. ZnPc thin films are known to suffer from a high density of trap states. Figure 4(b) shows the typical nonlinear behavior and hysteresis in the *j-V* curve expected in a thin film with a high trap density. Furthermore, Figure 4(b) shows a slight asymmetry in the *j-V* curve which occurs when charge injection from one of the contacts is better than from the other. Thus for positive bias, the current density values reach ~0.45 mA cm^{-2} at +5 V while they reach a mere 0.2 mA cm^{-2} at -5 V bias. In this case, the gold contact appears to be a better injector of holes into ZnPc compared to FTO, which is completely consistent with the higher work function of gold (~ 5 eV) vs. FTO (~4.6 eV). Another important thing to notice in Figure 4(b) is that the *j-V* curves in the dark and under solar light illumination are nearly identical, which clearly indicates the complete absence of photoconductivity. This, in turn, is due to the inability of photogenerated excitons in ZnPc to be dissociated.

Figure 4(c) shows the electrical characteristics of the FTO/ZnPc@Na-CNC/gold sandwich device, which are completely different from those of FTO/ZnPc/Au. The maximum currents are smaller than in ZnPc films but the non-linear behavior is smaller in absolute terms and the electrical behavior is more symmetrical. At zero-bias, non-zero current values are obtained in forward (-5 to +5 V) and reverse (+5 to -5 V) scans. The shape of the hysteresis no longer resembles typical trap-limited conduction wherein the maximum deviation or "spread" between the *j-V* curves correspond to the forward and reverse scans occurs at high values of bias. In Figure 4(c), the maximum "spread" occurs close to zero bias, which is indicative of charge storage and reminiscent of ferroelectric piezoelectric curves. This type of hysteresis is usually indicative of electrical bistability [39]. Photoconductivity is again negligible in the ZnPc@Na-CNC film.

Figures 4(d) shows that the two distinctive conductive states are discernable at a bias of +1.5 V. Occurrence of multi-conductive states at constant bias is known as electrical bi(multi)-stability or as "switching impact [40, 41]. After withdrawing the stimulation, if the contrast between two states continues for a long time, the device is defined as a "memory" [42], and if the difference disappears then at that point it may be a threshold [43] type of switching. We believe that the piezoelectric behavior of CNCs [44, 45] and the trap-mediated conduction in ZnPc [46] coincide to generate the observed bistability. The mechanism we propose is somewhat analogous to that of a ferroelectric random access memory (FRAM) [47]. The piezoelectric CNC acts as a field-dependent variable capacitor. During the forward scan, the CNC capacitor experiences charging and concurrently, traps in ZnPc are filled by holes injected from the contacts resulting in a higher effective drift mobility and a concomitantly increasing conductivity (nonlinear increase in current) [48, 49]. In the reverse scan, detrapping takes place and close to zero bias, trapped charge carriers in ZnPc would normally be completely depopulated but this is countered by the discharge of the CNC capacitor providing additional charge, hence allowing a higher than normal current at zero bias. Another potential interpretation of these results is that conjugation to CNC slows down the depopulation of trapped carriers by increasing the capacitance in the reverse scan (and hence a larger RC time constant) while not significantly affecting the rate of trap filling in the forward scan. It is well-known that phenomena such as trapping of charges at defect sites, percolating path formation, and distortion in the molecular configuration can result in such a switching phenomenon [50].

read and remove states. Several measurements were acquired in different areas of the device to ensure reproducibility. For the hysteresis plot in our device, a rise in voltage simultaneously increases the current and vice-versa. A short circuit current at 0 V is visibly observable in the *j-V* characteristics of the ZnPc@CNC device as displayed in figure 4 (c), particularly in the reverse scan. The existence of piezoelectric nanocrystals in the ZnPc@CNC devices is likely responsible for the memory device-like behavior giving rise to hysteresis and short circuit current at zero voltage which is absent in bare ZnPc device. Hysteresis is utilized by the memory devices by associating the conductive state +C and -C at zero voltage with a Boolean 1 and 0. For the FTO/ZnPc@CNC/Au device, the zero currents are quantified at +2.0 and -1.7 V in the forward and reverse sweeps respectively. These voltages are induced due to the storage of charges.

Figure 4. Counter-clockwise from top-left (a)Electrical measurements of metal/organic/metal (MOM) sandwiched device, Current density-voltage curve of (b) FTO/ZnPc/Au, (c) FTO/ZnPc@Na-CNC device. The arrow indicates the voltage sweep direction, transient analysis of (d) FTO/ZnPc@Na-CNC at +1.5 V, (e) FTO/ZnPc/Au device at +5 V, (f) Response of FTO/ZnPc/Au and FTO/ZnPc@CNC/Au samples at room temperature for 5 minutes cycling.

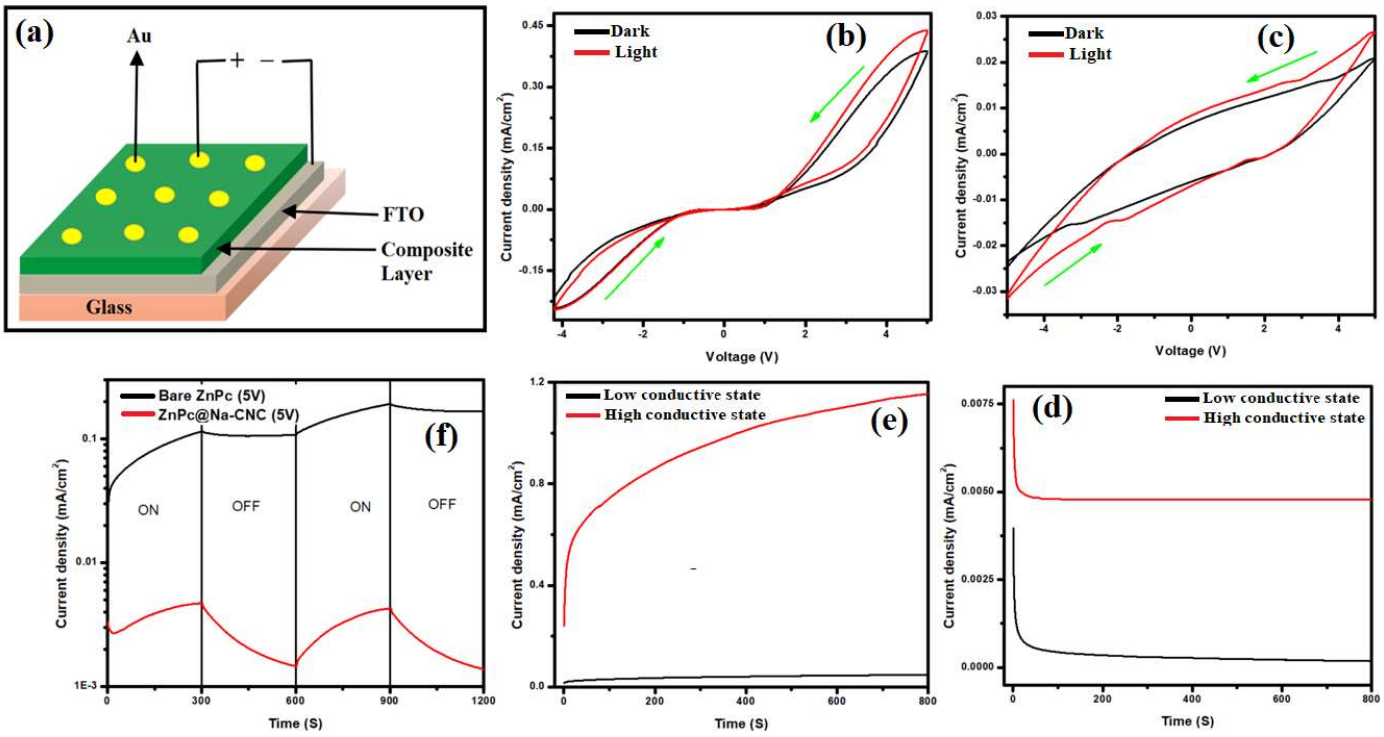

J-V measurements performed by sweeping the applied bias from $-V_{max}$ to $+V_{max}$ on a single-layer FTO/ZnPc@CNC/Au structure as a function of sweep rate did not show a variation in the hysteresis which indicates that the impact is genuine and not an artifact. The hysteresis shown by the device is sufficiently large, with a maximum difference of 0.028-0.03 mA/cm^2 at 1.0 V which is adequate to permit conclusive write,

The device takes a few seconds before reaching stability with a reliable contrast in current for both low and high conductive situations as shown in Figure 4 (d, e). The stability of our device under stress was recorded in the continuous bias condition without any significant device degradation. Although the mechanism is still beneath examination, it is believed that the conjugated CNC is playing a significant role in the sudden increment of infusion current and the withholding of high-level conductivity status once inclination is off. Trapped charges in the ZnPc@CNC are expected to be accountable for the noted electrical bistability and memory effect. The device is in an early stage of investigation, and it needs further study to define a detailed mechanism of bistability. This device uses CNC conjugated ZnPc as the active material and has huge potential for economical, large-area fabrication on flexible polymeric substrates for printed electronics.

The current at zero time is much larger for the device based on bare ZnPc in comparison to ZnPc@CNC based device during AM 1.5 G Sun illumination and is maintained throughout the dark, whereas in the case of ZnPc@CNC based device, the rate of increase and decrease in current during different modes is constant which is shown in figure 4(f) and this consistency is present throughout the device operation.

4. Conclusion

Octacarboxylated Zinc phthalocyanine was covalently grafted on the facade of Na-CNC and the occurrence of cellulose nanocrystals in the conjugate was validated by powder XRD patterns. DFT indicated strong wave function overlap between the CNC and ZnPc components. The HOMO and LUMO orbitals were spatially co-located on the CNC and ZnPc components instead of being spatially separated. Both ZnPc films and ZnPc@Na-CNC films exhibited hysteresis in their current voltage characteristics but the ZnPc@Na-CNC showed an enlarged hysteresis close to zero bias. Pristine ZnPc device exhibits a typical trap-mediated bistability with two different conductivity levels for the same bias depending on the scan direction (i.e. depending on whether traps are populated or depopulated) and the presence of CNCs in the ZnPc@CNC device is responsible for enlarging the hysteresis close to zero bias in the system. This electrical bistability is surmised to occur due to an interaction of the piezoelectric properties of CNCs with trap-mediated conduction in ZnPc. ZnPc@CNC is a new type of organic semiconductor with vast potential in printed and flexible electronics.

Acknowledgments

The authors like to acknowledge direct and indirect supports from the National Research Council Canada (NRC), Natural Sciences and Engineering Research Council of Canada (NSERC), FPInnovations Inc, Alberta Innovates—Technology Futures (AITF), University of Alberta Future Energy Systems (FES) and The Canada Foundation for Innovation (CFI). The University of Alberta NanoFAB staff member, Anqiang He is acknowledged for collecting TEM data. National Research Council staff member, Paul Concepcion is acknowledged for collecting FESEM images. The authors thank Dr. Wadood Hamad (FPInnovations) for valuable discussions and for providing Na-doped CNC.

References

[1] Ghoneim M and Hussain M 2015 Review on Physically Flexible Nonvolatile Memory for Internet of Everything Electronics *Electronics* **4** 424-79

[2] Ling Q-D, Liaw D-J, Teo E Y-H, Zhu C, Chan D S-H, Kang E-T and Neoh K-G 2007 Polymer memories: Bistable electrical switching and device performance *Polymer* **48** 5182-201

[3] Paul S, Kanwal A and Chhowalla M 2006 Memory effect in thin films of insulating polymer and C60 nanocomposites *Nanotechnology* **17** 145-51

[4] Ma D, Aguiar M, Freire J A and Hümmelgen I A 2000 Organic Reversible Switching Devices for Memory Applications *Advanced Materials* **12** 1063-6

[5] Chu C W, Ouyang J, Tseng J H and Yang Y 2005 Organic Donor-Acceptor System Exhibiting Electrical Bistability for Use in Memory Devices *Advanced Materials* **17** 1440-3

[6] Ma C Y, Li J Q, Zhang S Q, Duan W B and Zeng Q D 2021 Progress in self-assemblies of macrocycles at the liquid/solid interface *Nanotechnology* **32**

[7] Senthilarasu S, Velumani S, Sathyamoorthy R, Subbarayan A, Ascencio J A, Canizal G, Sebastian P J, Chavez J A and Perez R 2003 Characterization of zinc phthalocyanine (ZnPc) for photovoltaic applications *Applied Physics A* **77** 383-9

[8] Hu F Y, Zhang X M, Zhao Y B, Liu B, Duan W B, Wang C and Zeng Q D 2014 Substituent Effect on the Self-Assembled Structures of Two Carboxyl-Functionalised Phthalocyanine Derivatives on Highly Oriented Pyrolytic Graphite *Journal of Nanoscience and Nanotechnology* **14** 5375-9

[9] Shukla P, Yadav S, Patel M S, Kumar P, Kumar N and Kumar L 2021 The effects of cesium lead bromide quantum dots on the performance of copper phthalocyanine-based organic field-effect transistors *Nanotechnology* **32**

[10] Hammer S, Ferschke T, Eyb G v and Pflaum J 2019 Phase transition induced spectral tuning of dual luminescent crystalline zinc-phthalocyanine thin films and OLEDs *Applied Physics Letters* **115** 263303

[11] Shahiduzzaman M, Horikawa T, Hirayama T, Nakano M, Karakawa M, Takahashi K, Nunzi J-M and Taima T 2020 Switchable Crystal Phase and Orientation of Evaporated Zinc Phthalocyanine Films for Efficient Organic Photovoltaics *The Journal of Physical Chemistry C* **124** 21338-45

[12] Alam K M, Kumar P, Gusarov S, Kobryn A E, Kalra A P, Zeng S, Goswami A, Thundat T and Shankar K 2020 Synthesis and Characterization of Zinc Phthalocyanine-Cellulose Nanocrystal (CNC) Conjugates: Toward Highly Functional CNCs *ACS Applied Materials & Interfaces* **12** 43992-4006

[13] Bregado J L, Secchi A R, Tavares F W, de Sousa Rodrigues D and Gambetta R 2019 Amorphous paracrystalline structures from native crystalline cellulose: A molecular dynamics protocol *Fluid Phase Equilibria* **491** 56-76

[14] Plimpton S 1995 Fast Parallel Algorithms for Short-Range Molecular Dynamics *Journal of Computational Physics* **117** 1-19

[15] H. Sun P R a J R F 1998 The COMPASS force field-parameterization and validation for phosphazenes *Computational and Theoretical Polymer Science* **8** 229-46

[16] Ozaki T 2003 Variationally optimized atomic orbitals for large-scale electronic structures *Physical Review B* **67** 155108-5

[17] Bachelet G B, Hamann D R and Schlüter M 1982 Pseudopotentials that work: From H to Pu *Physical Review B* **26** 4199-228

[18] John P. Perdew K B, Matthias Ernzerhof 1996 Generalized gradient approximation made simple *PHYSICAL REVIEW LETTERS* **77** 3865-8

[19] Grimme S 2006 Semiempirical GGA-type density functional constructed with a long-range dispersion correction *J Comput Chem* **27** 1787-99

[20] Sinko R, Qin X and Keten S 2015 Interfacial mechanics of cellulose nanocrystals *MRS Bulletin* **40** 340-8

[21] Moreau C, Villares A, Capron I and Cathala B 2016 Tuning supramolecular interactions of cellulose nanocrystals to design innovative functional materials *Industrial Crops and Products* **93** 96-107

[22] Wang H, Sun Y, He W, Zhou Y, Lee S C and Dong F 2018 Visible light induced electron transfer from a semiconductor to an insulator enables efficient photocatalytic activity on insulator-based heterojunctions *Nanoscale* **10** 15513-20

[23] de Silva P and Corminboeuf C 2014 Simultaneous Visualization of Covalent and Noncovalent Interactions Using Regions of Density Overlap *J Chem Theory Comput* **10** 3745-56

[24] Matunova P, Jirasek V and Rezek B 2019 DFT calculations reveal pronounced HOMO-LUMO spatial separation in polypyrrole-nanodiamond systems *Phys Chem Chem Phys* **21** 11033-42

[25] Habibi Y, Lucia L A and Rojas O J 2010 Cellulose nanocrystals: chemistry, self-assembly, and applications *Chem Rev* **110** 3479-500

[26] Alam K M, Kar P, Thakur U K, Kisslinger R, Mahdi N, Mohammadpour A, Baheti P A, Kumar P and Shankar K 2019 Remarkable self-organization and unusual conductivity behavior in cellulose nanocrystal-PEDOT: PSS nanocomposites *Journal of Materials Science: Materials in Electronics* **30** 1390-9

[27] Ogunsipe A, Durmuş M, Atilla D, Gürek A G, Ahsen V and Nyokong T 2008 Synthesis, photophysical and photochemical studies on long chain zinc phthalocyanine derivatives *Synthetic Metals* **158** 839-47

[28] Li M-C, Wu Q, Song K, Lee S, Qing Y and Wu Y 2015 Cellulose Nanoparticles: Structure–Morphology–Rheology Relationships *ACS Sustainable Chemistry & Engineering* **3** 821-32

[29] Hassan M L, Moorefield C M, Elbatal H S, Newkome G R, Modarelli D A and Romano N C 2012 Fluorescent cellulose nanocrystals via supramolecular assembly of terpyridine-modified cellulose nanocrystals and terpyridine-modified perylene *Materials Science and Engineering: B* **177** 350-8

[30] Du L, Wang J, Zhang Y, Qi C, Wolcott M P and Yu Z 2017 Preparation and Characterization of Cellulose Nanocrystals from the Bio-ethanol Residuals *Nanomaterials (Basel)* **7**

[31] Ogbodu R O and Nyokong T 2014 Effect of bovine serum albumin and single walled carbon nanotube on the photophysical properties of zinc octacarboxy phthalocyanine *Spectrochim Acta A Mol Biomol Spectrosc* **121** 81-7

[32] Lewandowska A E and Eichhorn S J 2016 Quantification of the degree of mixing of cellulose nanocrystals in thermoplastics using Raman spectroscopy *Journal of Raman Spectroscopy* **47** 1337-42

[33] Gierlinger N. S M, Reinecke, A. and Burgert I. 2006 Molecular Changes during Tensile Deformation of Single Wood Fibers Followed by Raman Microscopy *Biomacromolecules* **7** 2077-81

[34] Barbara J. PaIys D M W v d H, Wim Briels and Dirk Feil 1995 Resonance Raman spectra of phthalocyanine monolayers on different supports. A normal mode analysis of zinc phthalocyanine by means of the MNDO method *Journal of Raman Spectroscopy* **26** 63-76

[35] Tackley D R, Dent G and Ewen Smith W 2000 IR and Raman assignments for zinc phthalocyanine from DFT calculations *Physical Chemistry Chemical Physics* **2** 3949-55

[36] Bao Z, Feng Y, Dodabalapur A, Raju V R and Lovinger A J 1997 High-Performance Plastic Transistors Fabricated by Printing Techniques *Chemistry of Materials* **9** 1299-301

[37] Sarı F A, Kazici M, Harputlu E, Bozar S, Koyun Ö, Sahin Y, Ugur N, Ince M and Günes S 2018 Zn Phthalocyanine Derivatives for Solution-Processed Small Molecule Organic Solar Cells *ChemistrySelect* **3** 13692-9

[38] Farag A A M, Yahia I S, Yakuphanoglu F, Kandaz M and Farooq W A 2012 Optical properties and the dispersion parameters of new zinc Phthalocyanine benzofuran derivative prepared by non-vacuum spin coating technique *Optics Communications* **285** 3122-7

[39] Salaoru I and Paul S 2012 Memory Effect of a Different Materials as Charge Storage Elements for Memory Applications *Advances in Science and Technology* **77** 205-8

[40] Bertin E, Halley D, Henry Y, Najjari N, Majjad H, Bowen M, DaCosta V, Arabski J and Doudin B 2011 Random barrier double-well model for resistive switching in tunnel barriers *Journal of Applied Physics* **109** 083712

[41] Collier C, Wong E, Belohradský M, Raymo F, Stoddart J, Kuekes P, Williams R and Heath J 1999 Electronically configurable molecular-based logic gates *science* **285** 391-4

[42] Scott J C and Bozano L D 2007 Nonvolatile Memory Elements Based on Organic Materials *Advanced Materials* **19** 1452-63

[43] Ielmini D and Zhang Y 2007 Analytical model for subthreshold conduction and threshold switching in chalcogenide-based memory devices *Journal of Applied Physics* **102**

[44] Miao C, Reid L and Hamad W Y 2021 Moisture-tunable, ionic strength-controlled piezoelectric effect

in cellulose nanocrystal films *Applied Materials Today* **24** 101082

[45] Wang J, Carlos C, Zhang Z, Li J, Long Y, Yang F, Dong Y, Qiu X, Qian Y and Wang X 2020 Piezoelectric Nanocellulose Thin Film with Large-Scale Vertical Crystal Alignment *ACS Applied Materials & Interfaces* **12** 26399-404

[46] Saleh A M, Hassan A K and Gould R D 2003 DC conduction processes and electrical parameters of the organic semiconducting zinc phthalocyanine, ZnPc, thin films *Journal of Physics and Chemistry of Solids* **64** 1297-303

[47] Ishiwara H 2012 Ferroelectric random access memories *Journal of nanoscience and nanotechnology* **12** 7619-27

[48] Mohammadpour A, Farsinezhad S, Wiltshire B D and Shankar K 2014 Majority carrier transport in single crystal rutile nanowire arrays *physica status solidi (RRL) – Rapid Research Letters* **8** 512-6

[49] Mohammadpour A, Wiltshire B D, Zhang Y, Farsinezhad S, Askar A M, Kisslinger R, Ren Y, Kar P and Shankar K 2017 100-fold improvement in carrier drift mobilities in alkanephosphonate-passivated monocrystalline TiO2 nanowire arrays *Nanotechnology* **28** 144001

[50] Beck A, Bednorz J G, Gerber C, Rossel C and Widmer D 2000 Reproducible switching effect in thin oxide films for memory applications *Applied Physics Letters* **77** 139-41